Additive Manufacturing Letters 16 (2026) 100352

Contents lists available at ScienceDirect

Additive Manufacturing Letters

journal homepage: www.elsevier.com/locate/addlet

Short Communication

Friction-induced distortion in binder jetted 316 L stainless steel: Experimental analysis, simulation, and compensation strategy

Marco Zago [a], Thomas Grippi [b], Elisa Torresani [b,*], Matteo Perina [c], Eugene A. Olevsky [b,d], Ilaria Cristofolini [a]

[a] Department of Industrial Engineering, University of Trento, Via Sommarive 9, 38123 Trento, Italy
[b] Mechanical Engineering, San Diego State University, San Diego, USA
[c] Mimest S.r.l., Via del Lavoro 30, 38063 Avio Italy
[d] NanoEngineering, University of California, La Jolla, San Diego, USA

ARTICLE INFO

Keywords:
Additive manufacturing
Metal binder jetting
Shrinkage on sintering
Dimensional accuracy and precision
Distortion
friction

ABSTRACT

This study investigates the origin of distortion during sintering of 316 L stainless steel components produced by binder jetting, focusing on friction between the sample and the support surface and on density inhomogeneity in the green state. A design of experiments (DoE) approach evaluates the influence of key printing parameters on the sintering behavior of two geometries with different through-hole sizes. Dimensional measurements, and density profiling, are performed in both green and sintered states. Sintering simulations use the Skorokhod-Olevsky viscous sintering (SOVS) model and include experimentally measured density gradients and frictional effects.

Results show that green density varies significantly (52% to 58%) depending on printing parameters, especially binder saturation, and exhibits directional dependence. These variations lead to measurable distortions during sintering. Simulations that include both friction and density gradients match experimental deformations with deviations below 4%. A compensation strategy that places parts on co-sintered 316 L support plates with interposed refractory particles reduces distortion to <1.5%.

This work demonstrates the combined role of friction and density gradients in sintering distortion and presents a practical method to improve dimensional accuracy in binder jetting.

1. Introduction

Distortion during sintering arises from multiple factors. One of the primary causes is inhomogeneous density distribution in the green state, which leads to localized differences in densification and, consequently, non-uniform volumetric shrinkage [1–4]. This shrinkage variation often results in shape changes and dimensional distortion. At high sintering temperatures, both ceramic and metallic materials exhibit low-viscosity behavior. When this rheological state is coupled with external influences such as gravity [5,6] and friction at the part-support interface [7], additional deformation may occur during sintering.

Numerous studies have focused on modeling sintering deformation. The Olevsky Continuum Theory of Sintering [8], and its linear-viscous formulation - the Skorokhod-Olevsky Viscous Sintering (SOVS) model - have been shown to predict densification and dimensional changes with high accuracy. Recent research has extended the application of the SOVS model to Binder Jetting (BJ) processes [6,7]. For instance, Torresani et al. validated the model using a T-shaped connector geometry, capturing the effects of gravity-induced loading with good agreement between experimental and simulated results [9]. In a related study, the same group applied an analytical model to quantify gravity-driven distortion in stereolithography-printed alumina components [6].

Paudel et al. developed a simulation framework for sintering deformation in metal BJ parts, incorporating both gravitational forces and a Coulomb friction coefficient of 0.5 [10]. Similarly, Borujeni et al. implemented the SOVS model along with a bilinear Mohr–Coulomb friction law, using a friction coefficient of 0.2 in one study [11], and 0.5 between 316 L stainless steel and an Al_2O_3 setter plate in another [12]. Zhang et al. reviewed the literature and found that many models use a constant Coulomb friction coefficient of 0.2; however, their own simulations achieved better agreement with experimental results using a higher coefficient of 0.9 [13]. This elevated value was attributed to

* Corresponding author.
E-mail address: etorresani@sdsu.edu (E. Torresani).

https://doi.org/10.1016/j.addlet.2025.100352
Received 15 October 2025; Received in revised form 23 December 2025; Accepted 29 December 2025
Available online 30 December 2025
2772-3690/© 2025 The Author(s). Published by Elsevier B.V. This is an open access article under the CC BY license (http://creativecommons.org/licenses/by/4.0/).

potential bonding between the sample and support surface during sintering in the absence of a ceramic setter. Similarly, Li et al. used a constant friction coefficient of 0.9 to simulate the initial bonding between the bottom surface of the printed part and the support, while a coefficient of 0.2 was used to model the relative movement during sintering [14]. Frictional effects have also been investigated in the context of Metal Injection Molding (MIM). Sahli et al. used a friction coefficient of 0.1 between 316 L parts and graphite supports [15], while Song et al. employed a coefficient of 0.5 between MIM-fabricated 316 L wheels and alumina supports [16].

Most of the literature has experimentally and numerically studied sintering distortion induced by gravitational forces or density gradients, while only a few studies have addressed distortion primarily induced by friction. Moreover, the literature lacks examples of compensation strategies to minimize friction-induced distortion.

In the present study, the influence of friction on densification, dimensional changes, and macrostructural evolution during the sintering of binder-jetted 316 L stainless steel components is investigated. A continuum-based sintering model, initially developed by Cabo Rios et al. [17–20] for cubic geometries, is adapted and extended to simulate the behavior of more complex parts under frictional loading conditions. The predictions of the FEM-embedded model are then compared with experimental results to evaluate its accuracy in capturing shape distortions and final geometry.

2. Materials and methods

2.1. Sample geometry

Two geometries were designed as shown in Fig. 1, having the same shape and dimensions except for the through-hole. Table 1 lists the nominal dimensions in both green and sintered states. The geometries were designed with sintered dimensions and then scaled to compensate for the expected anisotropic dimensional changes during sintering.

2.2. Design of experiments - printing

This study used AISI 316 L stainless steel powder, provided by Digital Metals (Sweden), now Markforged (USA), with a particle size of D10 8.1 µm D50 15.3 µm, D90 27 µm, as measured by laser diffraction particle size analyzer (GR01 Malvern Mastersizer 3000E instrument according to ASTM B822 Rev 2020).

The sample geometries were imported into Materialise software to populate the building chamber. Nine replicates of each geometry were positioned in the chamber, placed at three building levels, defined by the distance from the building platform. As shown in Fig. 1, a numeric marker was added to the vertical surface to facilitate sample identification during post-printing operations. All samples were aligned according to the reference system shown in Fig. 1, which means:

- X axis corresponds to the printhead injection direction.
- Y axis corresponds to the blade movement direction for leveling the powder bed.
- Z axis represents the building direction.

Table 1
Nominal dimensions in the green and in the sintered state of the two geometries. For dimension annotations see Fig. 1.

State	Geometry	LX Ext [mm]	LY Ext [mm]	LZ [mm]	LX Int [mm]	LY Int [mm]
Green	Thick	23.994	24.142	20.709	19.195	19.136
	Thin	23.994	24.142	20.709	21.595	21.728
Sintered	Thick	20	20	17	16	16
	Thin	20	20	17	18	18

The origin of the reference system in Fig. 1 corresponds to the first printed layer of the sample. The reference system is kept constant throughout the paper in all the figures.

A Digital Metal® DMP 2000 binder jet 3D printer was used for the prints. A design of experiments (DoE) methodology was employed to study the influence of printing parameters on the dimensional and geometrical accuracy of the sintered product. Specifically, an L9 orthogonal array was used in Taguchi's method to examine four printing parameters (factors) at three levels. This fractional factorial analysis was chosen as it requires 9 experiments, compared to 81 needed for a full factorial analysis (3^4).

The printing parameters investigated were:

- Printhead speed: the speed of the printhead as it injects binder onto the powder bed;
- Blade speed: the speed of the blade as it spreads and levels particles on powder bed;
- Shell thickness: as shown in Fig. 2, each printed layer includes a shell and a core area. The shell is created around the section perimeter

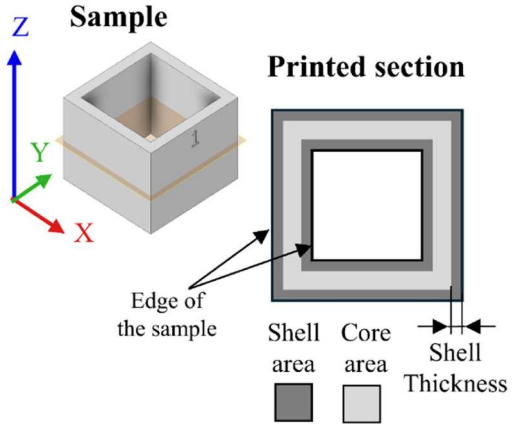

Fig. 2. Scheme of shell and core area.

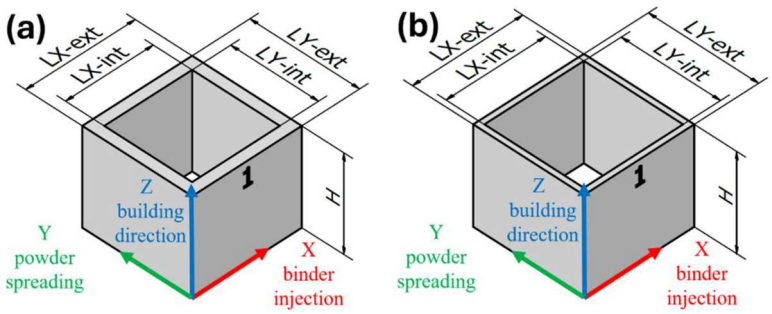

Fig. 1. Axonometric view and annotation convention of sample geometry (a) thick and (b) thin cubes.

based on the shell thickness. Binder saturation was kept constant in the shell area (dark body set to 8), while binder saturation in the core area varied according to the levels of dark body factor.

- Binder saturation grade: the binder content is controlled by a technological parameter named "dark body" by machine producer. Basically, it controls the percentage of pixels saturated by the binder. A dark body of 8 means all pixels are saturated, while a dark body of 3 indicates that 69 % of pixels are saturated [21].

Table 2 shows the permutation of factor levels in the nine experiments. The factor levels were selected within the range of standard values suggested by the machine manufacturer. Moreover, preliminary tests were conducted at the lowest blade speed, showing that below 20 mm/s the samples exhibited numerous defects. A maximum speed of 50 mm/s was also tested, and no significant defects were observed in the green samples. However, a maximum level of 38 mm/s was ultimately selected to prevent inhomogeneous packing density in the green state. All other printing parameters were kept constant: layer thickness (42 μm), image resolution (1200 DPI), and bed temperature (80 °C). The analysis of factor significance (ANOVA analysis) and the optimal combination of levels are presented in another works [22,23].

2.3. Post-printing operation and sintering

After printing, the building box was placed in a furnace and heated to 200 °C for 8 h to remove binder's aqueous component. This thermal process also induced crosslinking in the polymer component of the binder. Later, green parts were carefully extracted during de-powdering and subsequently sintered in a continuous furnace at 1370 °C under a fluxed pure hydrogen atmosphere. Full sintering cycle is confidential.

During sintering, the samples were placed on an alumina plate, except for the samples presented in Section 4.4. In that case, a plate printed using the same powder as the samples was used as support. Moreover, refractory powder was placed at the interface between the sample and plate surfaces to prevent bonding during sintering.

2.4. Dimensions measurement and evaluation of distortion

Three sample geometries for each experiment (one for each building level) were reconstructed in both the green and the sintered states using a coordinate measuring machine (CMM). A Hexagon DEA Global S 07–10–07 machine was used, with a maximum permissible error (MPE) of 2.2 + L/300 μm according to ISO 10,360–4. The machine was equipped with an HP-S-X1 probe and a stylus with a 2 mm spherical tip. Samples were fixed to the machine's working plane using a centering clamping system.

In the green state, the datum reference system, shown in Fig. 1, was defined by the two vertical planes: the X-Z plane for orienting the first datum, the Y-Z plane for locating the second, and top plane (X-Y) for blocking the third datum. Each surface was sampled with 9 points, and planes were reconstructed using a least squares method. Then, sample dimensions were calculated based on the distances between planes.

In the sintered state, vertical planes showed significant distortion near the base (first printed layer). For this reason, samples were rotated upside down as, shown in Fig. 3(a), allowing for a complete acquisition of the zone where distortion was most prominent.

The bottom plane (X-Y) of the sample was used for orienting the DRF. Secondly, X-Z and Y-Z midplanes were derived from the measurement of vertical planes and they were used for locating and blocking the datum reference frame. In the alignment procedure, 4 points were acquired for reconstructing each plane by using least squares method.

After alignment, a pattern of 180 points was acquired on each external surfaces, as shown in Fig. 3(b). The data was then post-processed in MATLAB 2024b to compute the difference between measured and nominal position of each point to highlight shape deformation during sintering Fig. 3(c).

Table 2
Matrix of experiments and factor's levels according to Taguchi model.

Experiment n	Printhead Speed [mm/s]	Binder saturation grade [-]	Blade Speed [mm/s]	Shell Thickness [pixel]
1	150	0	25	1
2	150	3	30	2
3	150	6	38	5
4	200	0	30	5
5	200	3	38	1
6	200	6	25	2
7	250	0	38	2
8	250	3	25	5
9	250	6	30	1

2.5. Density measurement

In the green state, density was determined by calculating the ratio between the sample's weight and its volume, as derived from dimensional measurements. Additionally, density gradients were examined along the X, Y, and Z axes, after sintering at 900 °C for 6 h in a tubular furnace (Carbolite STF 15/450). This low sintering temperature created necking between particles, resulting in minimal densification but sufficient mechanical strength to allow sample slicing. Sections were taken from different positions, as shown in Fig. 4. For these slices, density was measured according to the ASTM B962–23 standard, which involves multiple weights of samples in air, in air after oil impregnation, and in water after oil impregnation. Meanwhile, the density of samples sintered at 1370 °C were measured by water displacement methods, not using the oil impregnation.

In the sintered state, density was measured using the Archimedes method with a KERN ALJ 314–4A balance equipped with a water displacement kit. Relative density was calculated using a theoretical density of 7.95 g/cm^3, and densification was computed using Eq. (1).

$$\Gamma = \frac{\rho_s - \rho_g}{\rho_{th} - \rho_g} \tag{1}$$

3. Sintering modeling

This macro-scale sintering model, based on the Olevsky Continuum Theory of Sintering [8] and implemented in COMSOL™, couples thermal, mechanical, and densification phenomena to simulate the effects of external factors such as gravity and friction, along with sintering parameters like the thermal cycle, on component deformation and densification. The constitutive behavior is governed by the Eq. (2):

$$\sigma_{ij} = 2\eta_0\left[\varphi\dot{\varepsilon}_{ij} + \left(\psi - \frac{\varphi}{3}\right)\dot{e}\delta_{ij}\right] + P_L\delta_{ij} \tag{2}$$

Here, σ_{ij} denotes the stress tensor (Pa), representing the externally applied stresses, while $\dot{e}$ is the first invariant of the strain rate tensor (s^{-1}), corresponding to the volumetric shrinkage. η_0 is the shear viscosity of the fully dense material forming the powder (Pa·s), and δ_{ij} is the Kronecker delta. The normalized shear and bulk viscosity moduli, φ and ψ respectively, along with the effective sintering stress P_L (Pa), are all functions of porosity θ[20] (see the Appendix).

The rate of volume change in the porous material is described by the first invariant of the strain rate tensor, and can be correlated to the porosity evolution with the following mass conservation Eq. (3):

$$\dot{e} = \nabla_i\dot{u}_i = \left(\dot{\varepsilon}_x + \dot{\varepsilon}_y + \dot{\varepsilon}_z\right) = 3\dot{\varepsilon}_z = \frac{\dot{\theta}}{(1-\theta)} \tag{3}$$

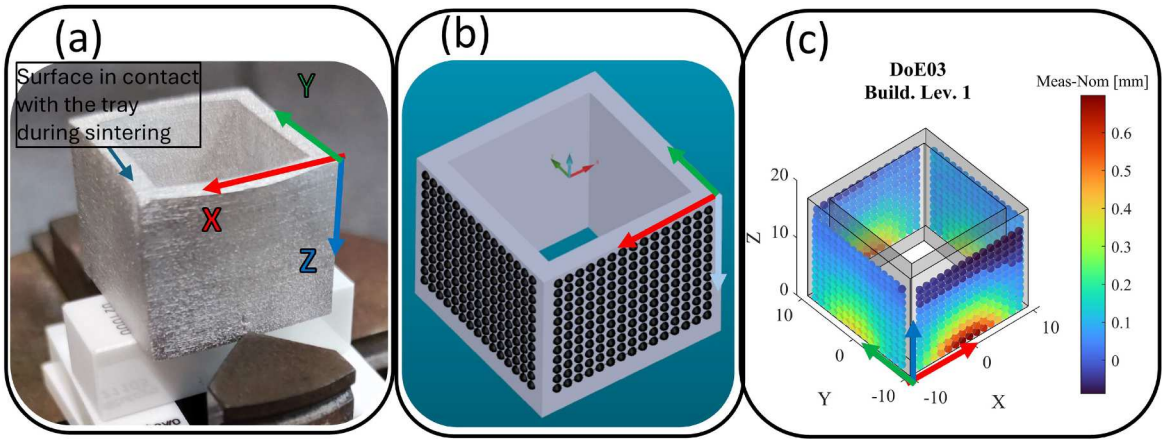

Fig. 3. (a) clamping system of sample to the CMM working plane. (b) pattern of points acquired on external surfaces of samples. (c) example of the deviation between experimental measurements and nominal point positions of nominal CAD or CAD extracted by the simulation.

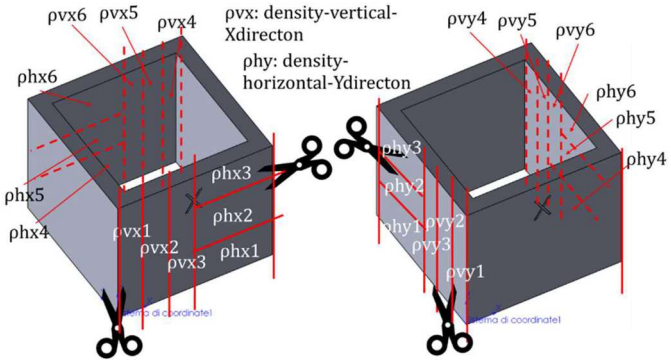

Fig. 4. The scheme of the slicing extracted by the pre-sintered samples to evaluate the density gradient in the green state.

3.1. Boundary conditions

Proper motion and equilibrium conditions were applied to the outer boundaries within the x–y–z coordinate system.

The gravitational force was defined as an external load and expressed as a function of porosity, allowing the equilibrium equation to be written as:

$$\nabla_j \sigma_{ij} + f_i = \nabla_j \sigma_{ij} + (1-\theta)\rho_{th}\vec{g} = 0 \tag{4}$$

Where f_i is the force per unit of mass, given in terms of density (kg m^{-3}) of the part and gravity acceleration vector $\vec{g}$ (m s^{-2}). Considering the application of gravity along the vertical direction, the equation can be simplified as [24]: $\sigma_z = -(1-\theta)\rho_{th}\vec{g}$.

At the interface between the lower surfaces of the components and the supporting structure, the following boundary conditions were imposed:

$$u_z = 0 \text{ and } \sigma_r = \mu\, \sigma_z \tag{5}$$

Here, σ_r represents the tangential surface stress resisting movement during densification or slumping, and following the classical Coulomb framework, it is related to the normal surface stress σ_z, induced by gravitational acceleration, via the friction coefficient μ. However, during sintering and densification, the interface does not remain in a purely static or purely sliding regime. To capture within a continuum framework the transition that occurs between sticking and sliding as relative motion and evaluate the frictional interaction between the simulated sintering component and the support, the following dynamic friction law was applied:

$$\mu = \mu_{dyn} + \left(\mu_{stat} - \mu_{dyn}\right) e^{\alpha_{dcf}|v_s|} \tag{6}$$

where the static friction coefficient μ_{stat} represents the maximum frictional resistance in the limit of vanishing slip velocity, corresponding to an interface in the sticking regime. The dynamic friction coefficient μ_{dyn} defines the asymptotic frictional resistance at finite slip velocities, where steady sliding occurs. The friction decay coefficient α_{dcf} controls the rate at which friction weakens as sliding initiates, thereby determining the sharpness of the transition between static and dynamic regimes. The slip velocity v_s represents the magnitude of the relative tangential velocity at the contact interface between the sintering component and the supporting surface. The values used in this work are reported in Table 3.

The proposed friction coefficients align with values reported in the literature for stainless steel, which typically range from 0.2 to 0.8, depending on surface roughness and load conditions [25,26].

While calculating the friction coefficient at high temperatures may seem straightforward, several studies have demonstrated that both the atmosphere and temperature significantly influence these values. In particular, it has been observed that friction coefficients tend to increase with rising temperatures [25,27,28].

3.2. Sintering model parameters experimental determination

The sintering model parameters were derived from dilatometric tests, as detailed in previous studies [20,29]. In these tests, the influence of gravity can be reasonably neglected due to the small size of the specimens. Consequently, Eq. (2) can be simplified to represent a pressure-less, isotropic case:

$$0 = 2\eta_0\left[\varphi\dot{\varepsilon}_z + \left(\psi - \frac{\varphi}{3}\right)3\dot{\varepsilon}_z\right] + P_L \tag{7}$$

Combining the continuity equation, Eq. (3), with the above Eq. (9) allows to derive the relationship which describes the porosity evolution during sintering:

$$\dot{\theta} = -(1-\theta)\frac{P_L}{2\eta_0\psi} \tag{8}$$

This equation characterizes the evolution of porosity as a function of porosity θ, effective stress P_L, normalized bulk viscosity ψ and the

Table 3
Friction coefficients assumed in this work.

μ_{stat}	μ_{dyn}	α_{dcf}
1.2	1	1

material's shear viscosity η_0. As previously noted, both P_L and ψ are dependent on porosity. The shear viscosity η_0 of the powder is temperature-dependent and is modeled using an Arrhenius-type expression. To account for the effect of delta-ferrite phase formation on the material behavior, a piecewise formulation—introduced in Eq. (A1)—is employed. In this formulation, the pre-exponential factor A_0 ($Pa{\cdot}s{\cdot}K^{-1}$) and activation energy Q ($kJ{\cdot}mol^{-1}$) are material-specific constants that must be experimentally determined.

These constants were previously derived from similar 316 L binder jetting (BJ) samples produced using the same printing and powder system, and sintered at various heating rates ranging from 2 to 15 °C/min [29]. Dilatometric analyses across these rates revealed that the kinetics of δ-ferrite formation had an impact on viscosity behavior. Consequently, the shear viscosity η_0 variation is considered for both phases in the present study. The values of the constants applied are provided in Table A1.

3.3. Comparison between sintering model and experimental results

Sintering simulation was employed for comprehending the origin of shape distortion occurring during sintering. The simulation was conducted on both geometries focusing on experiments DoE07 and DoE09. Three cases were investigated by using the SOVS sintering model. In case 1, dynamic friction coefficient was introduced, and a homogeneous density is assumed throughout the part. In case 2, friction was combined with the density gradient measured in the opposite sample' walls. The green density input values were determined by experimental procedure explained Section 2.5. Finally, a third case was investigated, assuming frictionless conditions between sample and support during sintering, but maintaining the density gradient. This simulation aims at clarifying the contribution of friction and density inhomogeneity on the origin of sintering distortion.

4. Results and discussion

Sintering distortion was measured across all samples. This deformation is then correlated with the green and sintered densities to explain the differences in shrinkage as a function of the printing parameters investigated through the design of experiments.

More detailed analysis was performed on samples DoE07 and DoE09, showing the minimum and maximum green densities, respectively, and the greatest differences in densification. Specifically, the following sections focus on these two printing conditions, discussing local density variation, and the comparison between sintering simulation and geometry reconstruction.

4.1. Geometry reconstruction and distortion analysis

Fig. 5 and Fig. 6 show the shape deformation for geometry *Thin* and *Thick*, respectively. Figures display samples printed using different printing conditions (DoE) and as a function of different building levels. Colored map represents the deviation of measured points from the nominal position in nominally sintered geometry as reported in Fig. 1 and Table 1.

Fig. 5 and Fig. 6 highlight non uniform deviation from nominal geometries across experiments. The deviation is poorly affected by the building levels, while it is significantly affected by printing parameters. Experiments 1, 4 and 7 showed the larger negative deviation while Experiments 3, 6 and 9 presented the larger positive deviation. This is attributed to binder content. Increasing the binder saturation grade, the shrinkage decreases during sintering as also reported in other literature works [22,30]. In both geometries, X-Z planes are significantly distorted, more than Y-Z planes. Looking from outside, X-Z surfaces present a convex shape deformation, whereas Y-Z surfaces have a slight concave shape, which is better highlighted in Fig. 7, or they are almost flat. Additionally, the distortion is in the bottom section of the parts and maximum occurred approaching the bottom plane. The distortion pattern repeats systematically in all *Thick* samples, while it changes in *Thin* samples, which also exhibit convex deformation on both the X–Z and Y–Z surfaces.

Hofmann et al. observed similar distortion on cube of 10 × 10 mm while symmetric distortion was found on similar geometries printed in the present work [31]. They attributed the deformation to frictional force between sample and support. Basically, during sintering, material

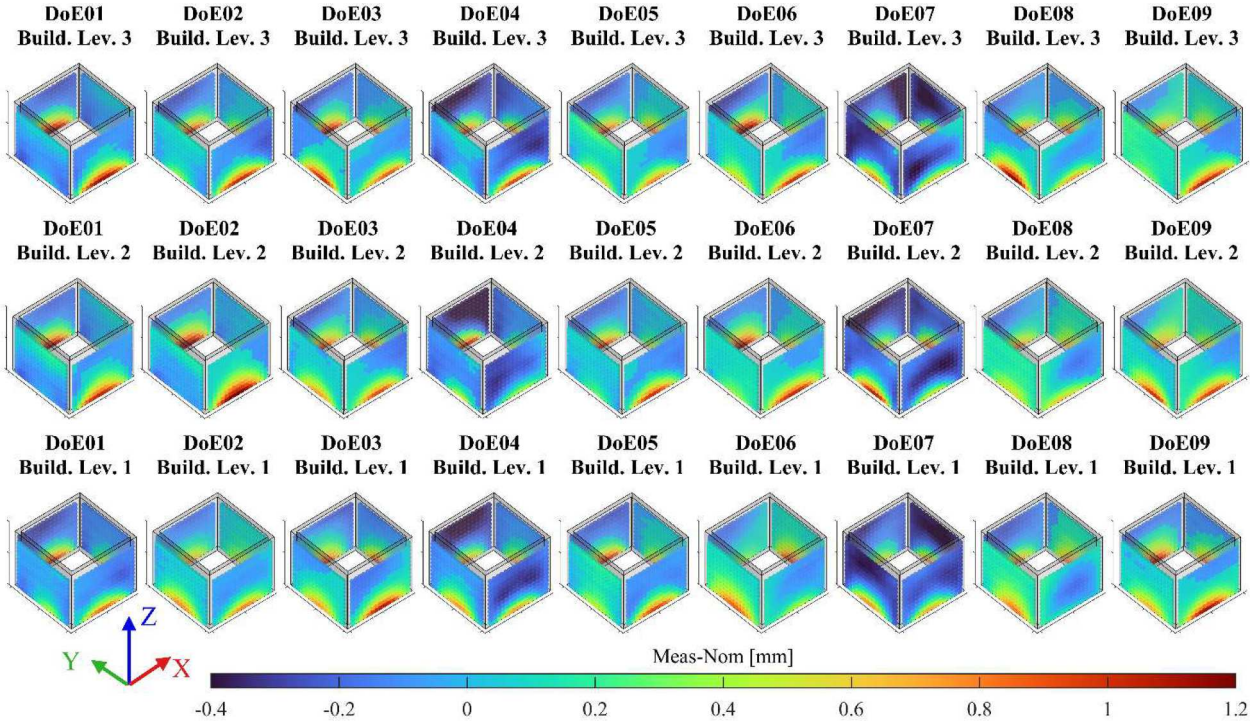

Fig. 5. Shape deformation in the sintered state of thin geometry as a function of the experiment (DoE) and building level (1,2,3).

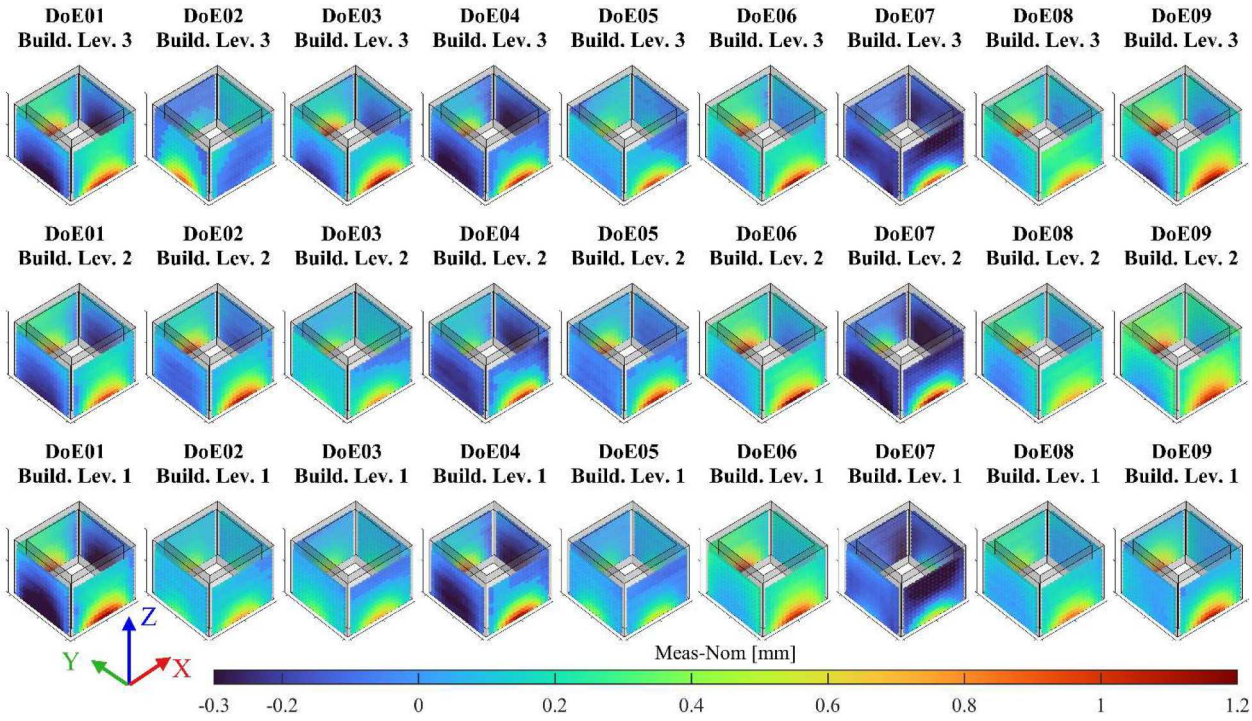

Fig. 6. Shape deformation in the sintered state of thick geometry as a function of the experiment (DoE) and building level (1,2,3).

shrinkage produced a relative movement between sample and support. The frictional force acted opposite to the sample displacement producing a virtual constraint to free-sintering.

4.2. Density measurement in the green and sintered state

Fig. 8 shows the green, sintered density and densification parameter as a function of experiment number (DoE) and building levels for geometry *Thick* and *Thin*.

Generally, no significant differences were found when comparing the two geometries. In the green state, *Thick* samples exhibited higher green density than *Thin* ones, although the scatter bands are virtually overlapping. In the sintered state, *Thin* samples showed slightly higher density. Literature generally reports that as green density decreases, sintered density increases [22,30]. Additionally, larger the part volumes are associated with lower sintered density due to the closure of surface porosity, which prevents the gas evacuation from pores in the inner part of the material [32]. Generally, samples are almost fully densified after sintering. All batches presented similar sintered density between 98 % and 100 % as shown in Fig. 8(c)-(d). Conversely, green density (Fig. 8 (a)-(b)) is significantly affected by the printing parameters, especially binder content. Increasing the binder saturation grade, green density increases as exhaustively explained in [22]. Green density is not significantly affected by the position in the building plane (X-Y coodinates); however, it is slightly influenced by the printing level (Z coordinate) in the way that sample printed closer to the building platform (level 1) presented higher green density in comparison to last printed samples (level 3). This outcome has been observed in other works and it has been related to the powder compaction during the powder spreading stage [1,33]. These variations can explain the slight difference in distortion intensity as a function of experiments and printing level showed in Fig. 5 and Fig. 6. The lower initial green density is associated with higher densification, which results in slightly higher distortion during sintering.

Green density gradient was also evaluated by cutting some slices in pre-sintered samples as shown in Fig. 4. The results are displayed in Table 4 for experiments 7 (DoE07) and 9 (DoE09).

Generally, slightly higher green density was found on plane XZ (powder spreading section) than YZ (binder injection section) Several authors characterized porosity distribution generated by printing operation using metallographic analysis [18,34] or micro-computer tomography [35–37]. These studies showed a periodicity on pores which can be attributed to layering fabrication. In addition to the layered-porosity along printing direction (Z), pores bands aligned with binder deposition direction have been found on metallographic section cut parallel to the printing plane (X-Y) [18,38]. Authors assumed that these bands were produced by the ballistic impact of binder droplets on powder bed as observed monitoring binder deposition using high-speed X-ray imaging [39,40].

4.3. Simulation results

Fig. 9 reports the sintering simulations according to the three scenarios, as described in Section 3.3. Fig. 9(a) displays the deformation assuming static and dynamic friction conditions between the sample and the support, while maintaining a homogeneous initial density. This leads to a symmetrical deformation pattern influenced by frictional forces, which partially replicates the experimental deformation shown in Fig. 7, especially for some *Thin* samples.

Fig. 9(b) reports the deformation combining both friction conditions and initial density differences in the opposite walls case (2-by-2 configuration). The sintering deformation is clearly asymmetrical, presenting an hourglass-like profile. This outcome closely mirrors experimental results for both tested geometries, validating the critical role of the interplay between friction and initial density gradients in governing sintering behavior.

Finally, Fig. 9(c) displays the sintering deformation obtained assuming frictionless condition between sample and support, while maintaining the density gradient in the initial condition. The simulation shows homogeneous densification with no asymmetry in the final shape, resembling the behavior observed during sintering with a base plate, as further described in Section 4.4.

Fig. 10 and Fig. 11 compare the deviation between experimental and simulation results in scenario number 2, for geometry *Thick* in

experiments DoE07 and DoE09, moreover Table 5 and Table 6 quantify the maximum distortion obtained by CMM measurement and simulation. In both experiments, simulation deformation of the bottom plane mimics the shape of samples after sintering, proving the contribution of friction and density inhomogeneity in the origin of sintering distortion. The colored map shows the deviation between the experimental and numerical results. Essentially, colors indicate the deviation between measured and nominal point coordinates, deriving nominal point coordinates from the CAD extracted by the simulation. Generally, the sintering simulation slightly underestimates the deformation along Y direction (XZ planes), mostly close to the bottom plane. This difference is attributed to the experimental limits on quantifying density inhomogeneity by using other samples, not strictly the samples sintered and measured. For this reason, slight discrepancy in actual and assumed density inhomogeneity could have produced the deviation reported here.

Further analysis of Fig. 10 and Fig. 11 displays that the simulation of experiment DoE09 provides a lower discrepancy with respect to DoE07. As previously discussed, the actual estimation of density in the green state is challenging and significantly affects numerical results. The use of more advanced techniques, like micro-CT, can improve density measurement in the green state and improve data overlapping.

4.4. Compensation of frictional deformation

The use of supports to counteract distortion during sintering is poorly described in the literature [41,42], though it is often recommended in the design guidelines provided by printer manufacturers and part producers [43–46].

As explained in [41], the approach involves printing both supports and parts using the same material and coupling them for sintering. To prevent bonding during sintering, refractory particles are placed between the support and part surfaces. The use of supports can effectively mitigate both gravity-induced distortions and friction-induced distortions since supports and parts shrink simultaneously during sintering. The absence of relative movement between the support base and the sintering samples during sintering, eliminates the frictional forces. It is worth noting that, supports are not required during BJ printing operations unlike in laser-based AM technology.

Fig. 12 presents the results of applying this strategy to the *Thick* geometry investigated in this study. Fig. 12(a) compares these experimental results with those from sintering simulation case 3, which incorporates density inhomogeneity and assumes frictionless condition. CMM measurements highlight an almost perfect overlap between experimental and numerical results on the XZ planes, while the simulation slightly overestimates shrinkage on the YZ planes. This discrepancy likely arises from the model's isotropic-shrinkage assumption, despite the anisotropic shrinkage behavior observed in actual BJ

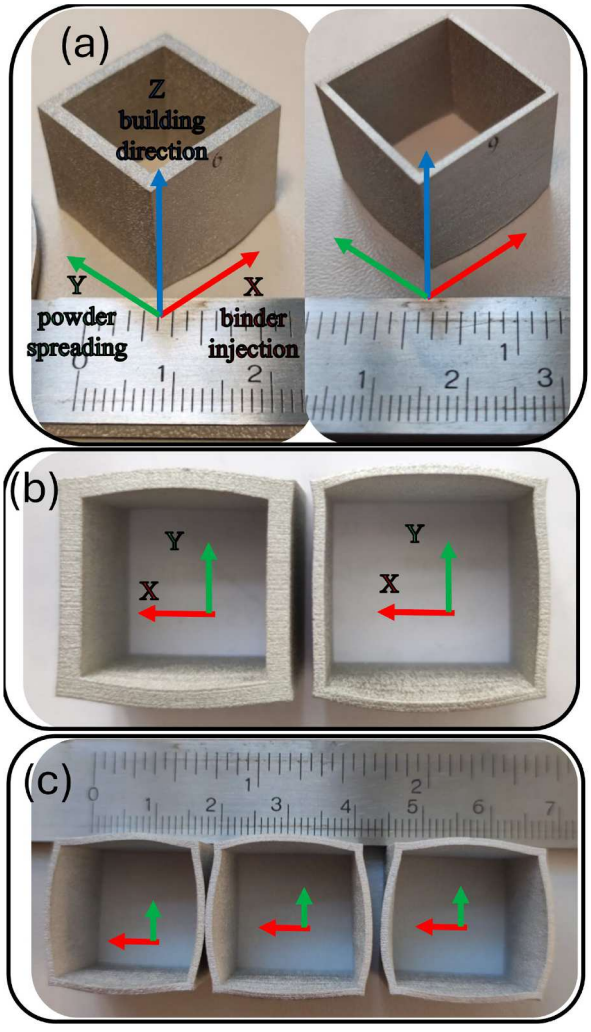

Fig. 7. Sintering deformation of the thick and thin samples (a) overall view, (b) bottom view, (c) different deformations of thin samples.

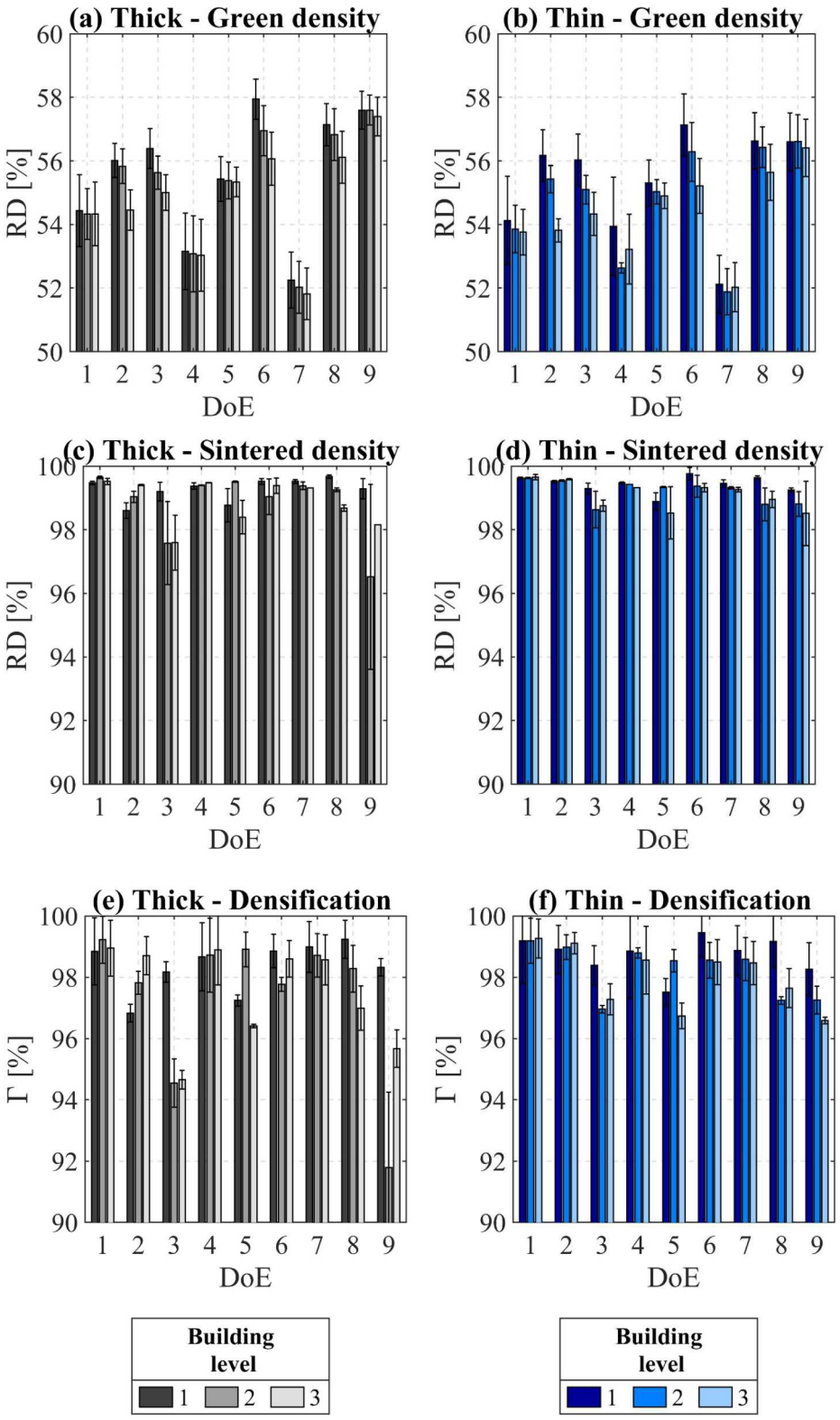

Fig. 8. Green density, sintered density and densification as a function of the experiment (DoE) and building level (1, 2, 3). (a) green - thick, (b) green - thin, (c) sintered – thick, (d) sintered - thin. (e) densification – thick. (f) densification – thin.

products. Fig. 12(b) shows the deviation from nominal CAD geometry, with the sintered dimensions reported in Table 1. The maximum deviation is on the order of ±0.15 mm (1.5 % of linear dimension), demonstrating that the cube geometry is preserved after sintering, with only marginal deformation induced by friction near the sample's base. These findings highlight a straightforward yet effective approach to prevent friction-induced deformation during sintering.

5. Conclusions

This work investigated the sintering deformation of 316 L manufactured via binder-jetting technologies. A design-of-experiments

Table 4
Density measurements in XZ and YZ section of pre-sintered samples and deviation from nominal values.

Experiments	Average density and standard deviation [%]		Deviation from average value [%]	
	XZ plane	YZ plane	XZ plane	YZ plane
DoE07	53.21 (0.97)	52.65 (0.41)	0.53 %	−0.53 %
DoE09	58.42 (0.87)	57.66 (0.38)	0.65 %	−0.65 %

methodology was employed to study the influence of printing parameters on sintering deformation. Two cubic geometries were designed, each including a square through-hole of different size. Samples were located at different height levels in the build box to study the effect of printing position. Before and after sintering, sample geometries were reconstructed using a coordinate-measuring machine. Specifically, sintered samples exhibited high distortion compared to the nominal geometry, which is attributed to friction-induced deformation and density inhomogeneity in the green state. Sintering simulations were conducted using the SOVS model to validate these hypotheses.

Here is a list of the main findings:

- Density: Experimental measurements show a significant green density variation across experiments, as a function of building level, and as a function of the printing direction.
  - Effect of process parameters: green density ranges between 52 % to 58 % in the nine batches. Binder saturation is found to be the most critical parameter affecting green density and shrinkage. Basically, higher binder saturation produces higher green density, while other printing parameters are not significant for either sintering densification or deformation.
  - Effect of printing level: In the green state, density slightly decreases with increasing distance from the build platform, but this trend disappears after sintering. The difference in the green state is attributed to powder compaction by the blade during powder spreading.
  - Effect of building direction: Slightly higher green density was found along the powder-spreading direction than the binder-injection direction in a range between 0.53 % and 0.65 %.
- Sintering distortion: Samples were distorted after sintering, especially near the bottom surface. This result is attributed to the influence of friction between the sample and the sintering-tray surfaces, and to density inhomogeneity in the green state:
  - Friction-induced deformation: The sintering model demonstrated the impact of friction on the origin of distortion. Static and dynamic friction models were employed in simulation.
  - Density-induced distortion: Furthermore, sintering simulation confirmed the critical effect of density variation on the non-symmetric deformation of samples. Comparison between the sintering model and experimental results highlights a maximum deviation of 3.85 % along the powder-spreading direction and 2.34 % along the binder-injection direction.
- Friction-compensation approach: A compensation approach was successfully tested by placing samples on a 316L-printed support plate and inserting refractory particles between them to prevent bonding during sintering. Geometric reconstruction showed

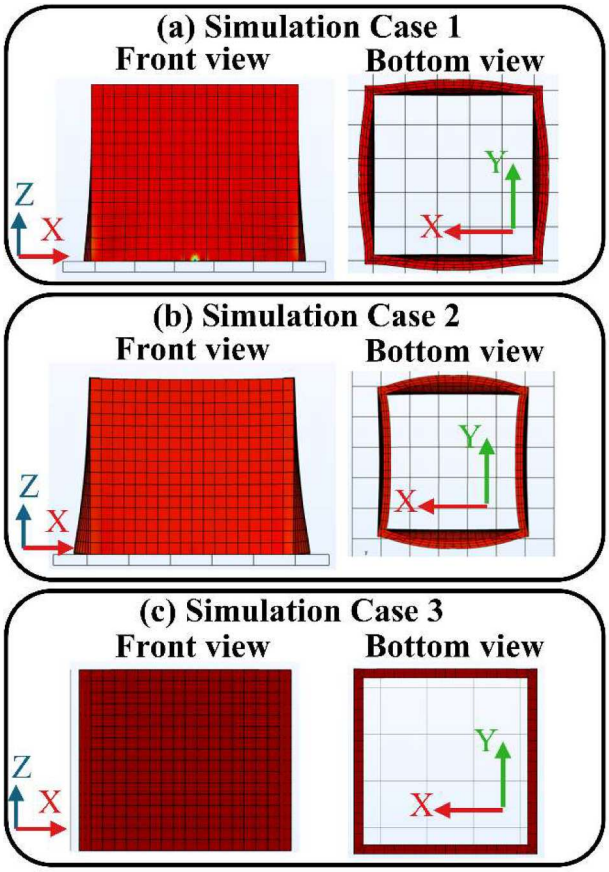

Fig. 9. Shape changes during sintering resulting in different simulation scenarios. (a) Case 1: homogeneous density and friction condition between sample and support. (b) Case 2: inhomogeneous density distribution and friction condition. (c) Case 3: inhomogeneous density distribution and frictionless condition.

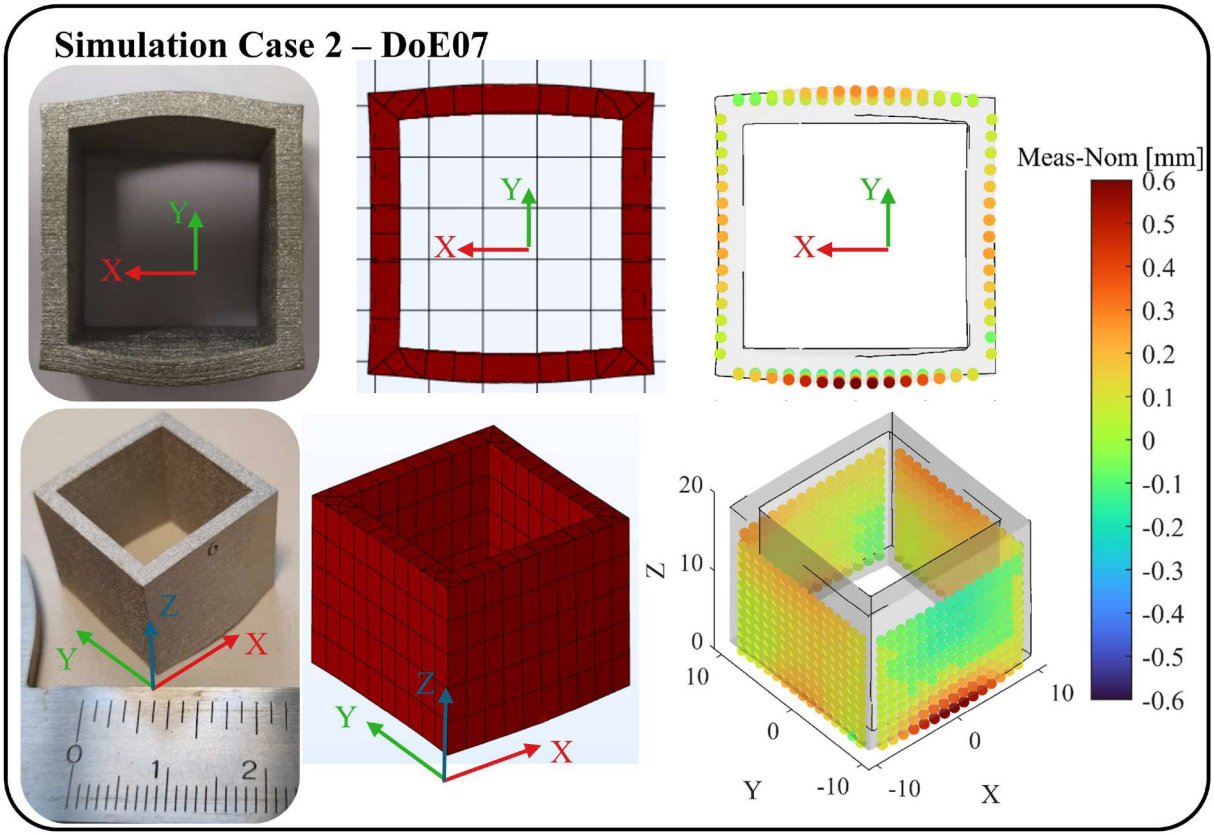

Fig. 10. Deviation between experimental and sintering simulation of thick geometry. from left to right: bottom and overall view of the samples, of the simulation, and colored map showing the deviation of measured points acquired by CMM from nominal points of the CAD obtained by the simulation - experiment DoE07.

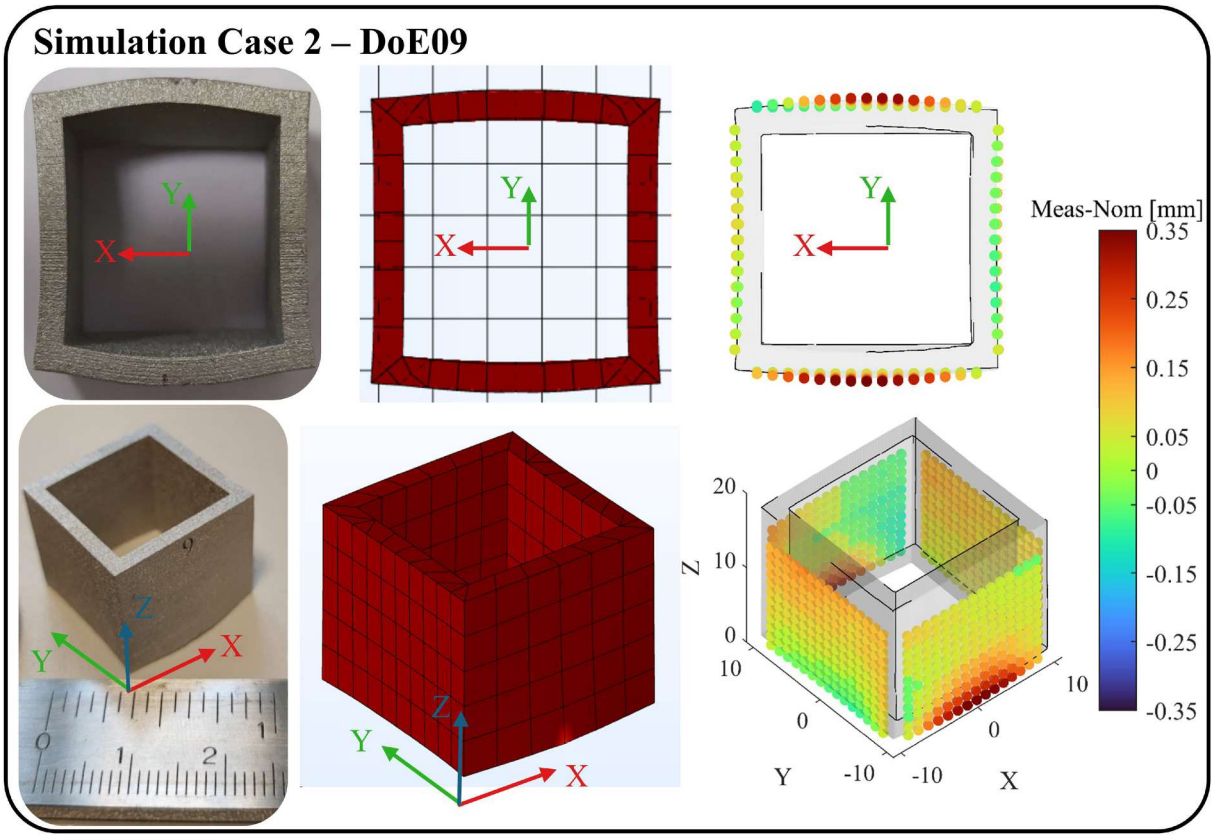

Fig. 11. Deviation between experimental and sintering simulation of thick geometry. From left to right: bottom and overall view of the samples, of the simulation, and colored map showing the deviation of measured points acquired by CMM from nominal points of the CAD obtained by the simulation - experiment DoE09.

Table 5
Comparison between experimental and simulation results of the maximum linear dimensions in the distorted bottom plane of experiment DoE07.

Sample DoE07	LX	LY
Experiment	19.52 [mm]	21.98 [mm]
Simulation	19.063 [mm]	21.134 [mm]
(Simulation- Exp)/Exp	2.34 %	3.85 %

Table 6
Comparison between experimental and simulation results of the maximum linear dimensions in the distorted bottom plane of experiment DoE09.

Sample DoE09	LX	LY
Experiment	19.58 [mm]	22.34 [mm]
Simulation	19.539 [mm]	21.842 [mm]
(Simulation- Exp)/Exp	0.21 %	2.23 %

negligible distortion and a maximum deviation of ±0.15 mm (1.5 % of linear dimension) from the nominal geometry. The sintering model slightly overestimates shrinkage in the X direction (+0.2 mm), likely due to the model's isotropic-shrinkage assumption.

In summary, this study provides an analysis of sintering deformation in binder-jetted 316 L components, highlighting the critical roles of green density variation and friction at the part-support interface. Through combined experimental measurements and validated sintering simulations, it demonstrates that even small differences in green density can significantly influence final geometry. The work further introduces a practical compensation strategy using co-sintered supports and refractory particles, effectively mitigating distortion. These findings advance the understanding of deformation mechanisms in metal binder jetting and offer a validated pathway for improving dimensional and geometrical accuracy in sintered parts.

Statements and declarations

Funding: The project is financed by Provincia Autonoma di Trento, L. P. 13/12/1999, n. 6, Art. 5: Aiuti per la promozione della ricerca e sviluppo. The authors are grateful to the whole staff of Mimest s.r.l. for producing the samples and fruitfully cooperating.

The support by the National Science Foundation (Award number: DMR-2119,832) is gratefully appreciated.

CRediT authorship contribution statement

Marco Zago: Writing – review & editing, Writing – original draft, Investigation, Data curation. **Thomas Grippi:** Writing – review & editing, Software, Data curation. **Elisa Torresani:** Writing – review & editing, Supervision. **Matteo Perina:** Writing – review & editing.

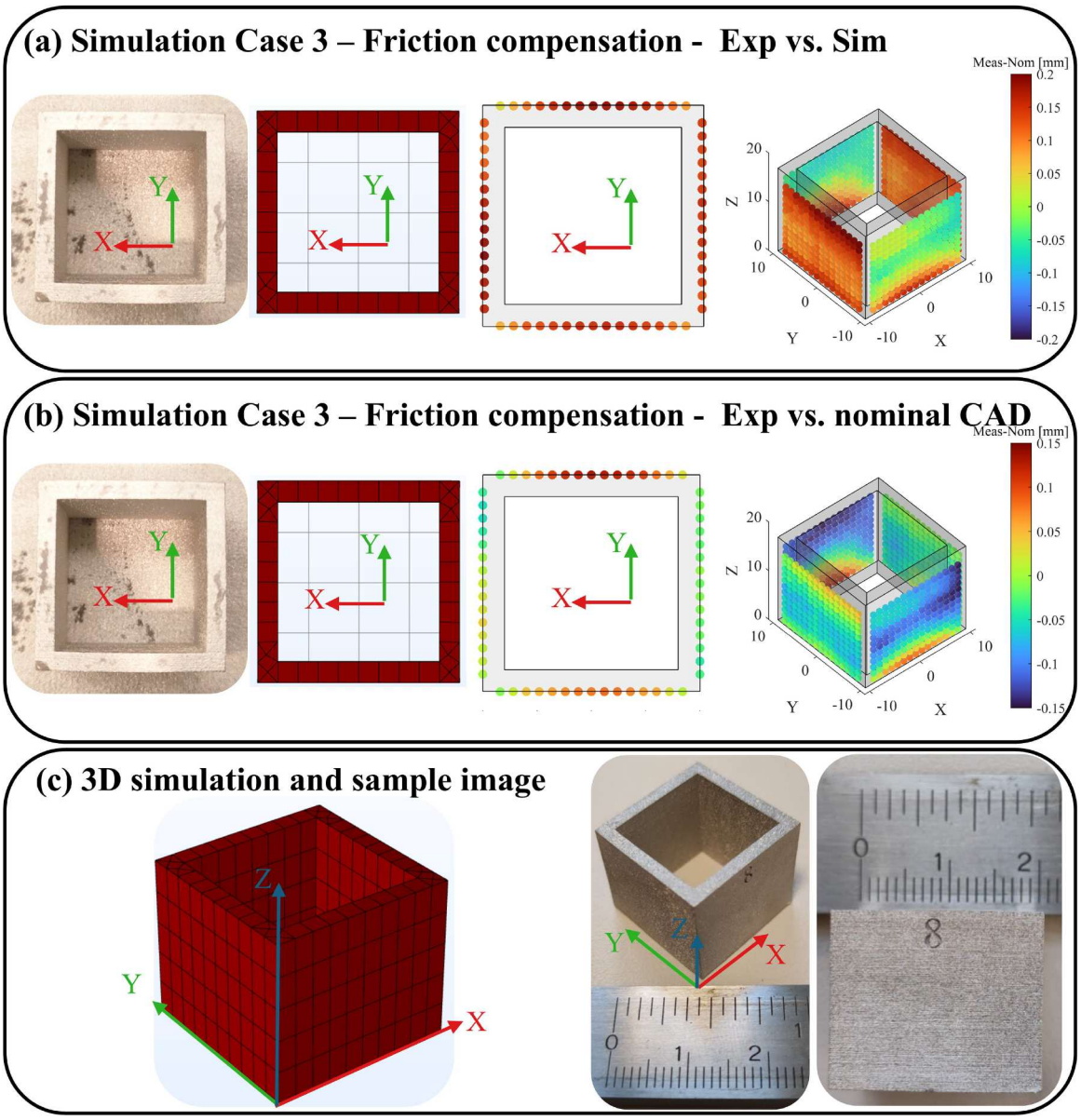

Fig. 12. Shape deviation of sample Thick produced by using friction compensation approach. From left to right: Bottom view of the samples, of the simulation, and colored map showing the deviation of measured points acquired by CMM from nominal points of the CAD. (a) comparison of Experimental and simulation results. (b) Deviation between experimental measurement and nominal CAD file. (c) 3D view of the simulation results and picture of the actual sample.

Eugene A. Olevsky: Writing – review & editing, Supervision. **Ilaria Cristofolini:** Writing – original draft, Supervision.

Declaration of competing interest

The authors declare that they have no known competing financial interests or personal relationships that could have appeared to influence the work reported in this paper.

Appendix

A1. Simulation model appendix

A piecewise Arrhenius-type function, previously proposed [24], was used to describe the viscosity parameter η_0, introducing a defined transition temperature to differentiate the material's behavior across two distinct thermal regimes [9,24].

$$\eta_0 = A_i T \exp\left(\frac{Q_i}{RT}\right) \begin{cases} i = 1 \rightarrow A_1\ Q_1, & if\ T < T_T \\ i = 2 \rightarrow A_2\ Q_2, & if\ T \geq T_T \end{cases} \tag{A1}$$

$$where:\ T_T = \frac{Q_2 - Q_1}{R \ln\left(\frac{A_1}{A_2}\right)} \tag{A2}$$

i	$A_i/\alpha\left[s\ m^{-1}K^{-1}\right]$	$Q_i\left[K\ J\ mol^{-1}\right]$	$T_T[K]$
1	8.993	201.7	1583.62
2	5.335e-32	1178.7	

Expressions as a function of porosity for sintering stress and normalized bulk and shear viscosities:

$$P_L = \frac{3\alpha(1-\theta)^2}{r_g} \tag{A3}$$

$$\varphi = (1-\theta)^2 \tag{A4}$$

$$\psi = \frac{2}{3}\frac{(1-\theta)^{11.35}}{\theta^{0.49}} \tag{A5}$$

In the final expression, the effective sintering stress—also referred to as the Laplace pressure—is directly proportional to the material's surface tension α (J·m^{-2}), which serves as the primary driving force for sintering, and inversely proportional to the average grain radius r_g (m).

The kinetic equation proposed by Olevsky [25] can be used to describe the evolution of the grain growth during the sintering process:

$$\frac{dr_g}{dt} = \frac{k_0}{3r_g^2}\left(\frac{\theta_c}{\theta+\theta_c}\right)^{\frac{3}{2}} exp\left(\frac{Q_g}{RT}\right) \tag{A4a}$$

In this non-linear equation, the temperature dependence of grain growth kinetics is captured by the pre-exponential factor k_0 (m^3 s^{-1}) and the activation energy Q_g (kJ mol^{-1}). The evolution of porosity is influenced by the critical porosity θ_c. which represents the threshold at which pore depinning from the grain boundaries significantly affects both grain growth and densification kinetics. These parameters were experimentally determined in a previous study by [20] and are summarized in Table A1.

Table A1
Parameters for Eq. (A4) identified for binder jetted samples made by 316 L ([20]).

($m^3\ s^{-1}$)	Q_g (kJ mol^{-1})	θ_c
$2.97{\cdot}10^{-22}$	164.8	5.20 %

A2. Metallographic analysis and XRD

In the sintered state, residual porosity was evaluated by optical micrographs in *Thick* samples printed in experiments number 7 (DoE07) and number 9 (DoE09). These samples were chosen since they presented the lowest and the highest green density, respectively. Fig. A1 shows X-Z sections, while Fig. A2 displays Y-Z sections.

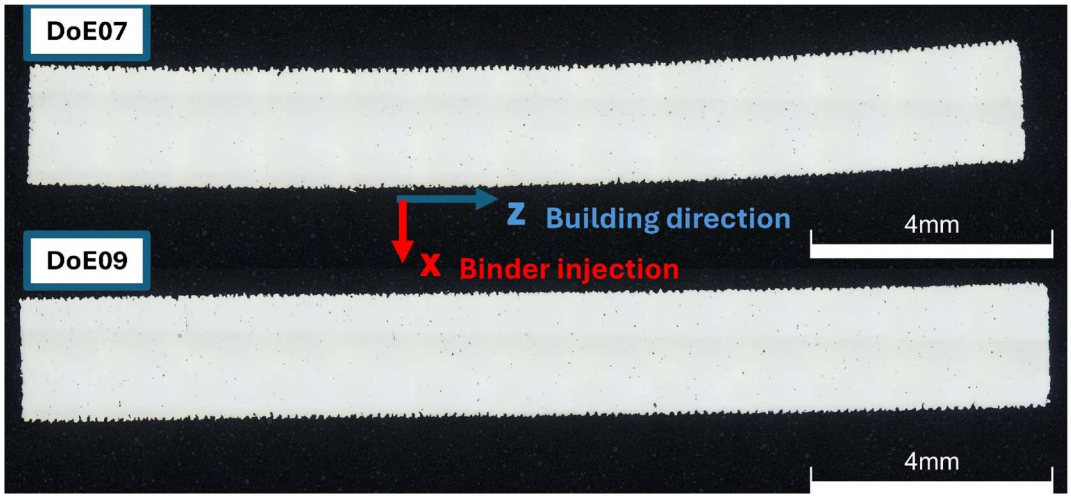

Fig. A1. Optical micrograph of X-Z plane of samples from experiments number 7 (DoE07) and number 9 (DoE09).

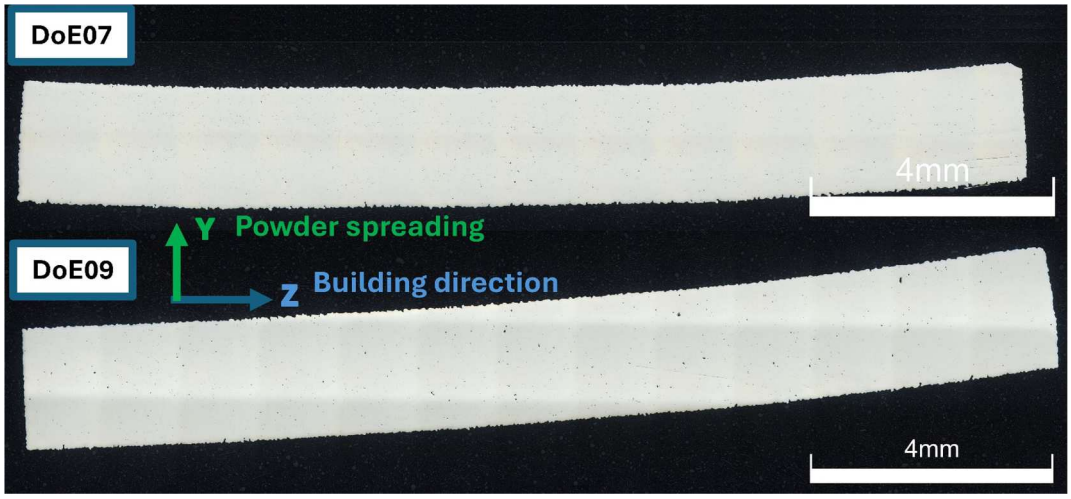

Fig. A2. Optical micrograph of Y-Z plane of samples from experiments number 7 (DoE07) and number 9 (DoE09).

Generally, the porosity distribution is virtually uniform when comparing the X-Z and Y-Z sections and when comparing DoE07 with DoE09. No significant gradient was observed as a function of building direction (Z). DoE09 exhibited slightly higher porosity compared with DoE07, which aligns with the density measurements showed in Fig. 8. The etched microstructure is displayed in Fig. A3 for both the X-Z and Y-Z sections as well as DoE07 and DoE09.

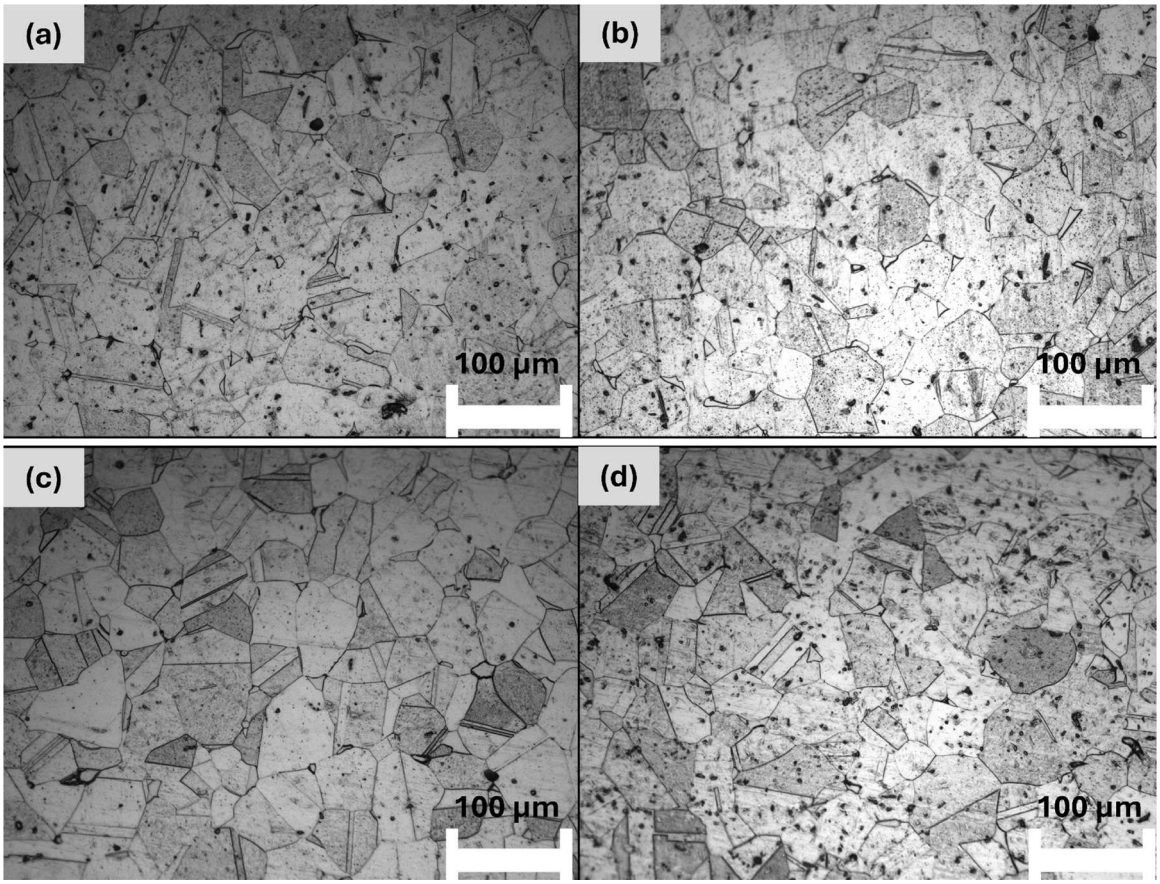

Fig. A3. Etched microstructure of (a) DoE07 – section X-Z, (b) DoE09 – section X-Z, (c) DoE07 - section Y-Z, (d) DoE09 - section Y-Z.

Fig. A3 illustrates a nearly identical microstructure in both samples across the different planes. The predominant phase is austenite, with small amounts of ferrite and twinning also observed. A few spots of delta ferrite are distinguishable within the microstructure; however, these are below the detection threshold of the XRD analysis (Fig. A4). In conclusion, the printing process does not significantly affect the microstructure following the sintering process. Although differences in green density result in variations in densification and dimensional shrinkage, the final microstructure remains consistent after sintering.

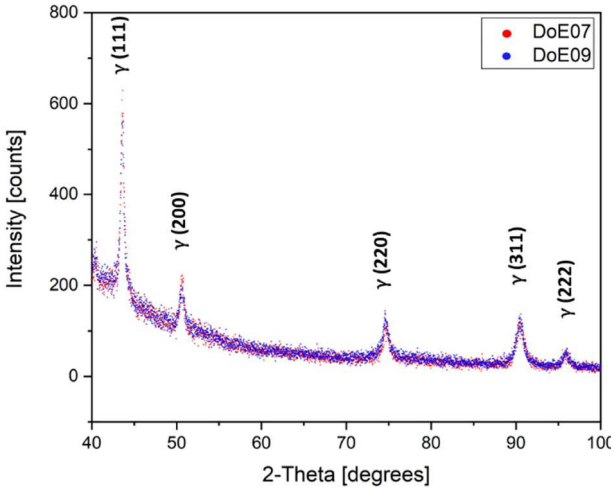

Fig. A4. XRD analysis.

Data availability

The data are available from the corresponding author on reasonable.

References

[1] B.J. Paudel, A.C. To, Spatial green density variation and its effect on distortion prediction in binder jet additive manufacturing, Addit. Manuf. 98 (2025) 104640, https://doi.org/10.1016/j.addma.2025.104640.
[2] Y. Lee, P. Nandwana, S. Simunovic, Powder spreading, densification, and part deformation in binder jetting additive manufacturing, Prog. Addit. Manuf. 7 (2022) 111–125, https://doi.org/10.1007/s40964-021-00214-1.
[3] B.J. Paudel, H. Deng, A.C. To, A physics-based data-driven distortion compensation model for sintered binder jet parts considering size effects, Addit. Manuf. 68 (2023) 103517, https://doi.org/10.1016/j.addma.2023.103517.
[4] E. Stevens, S. Schloder, E. Bono, D. Schmidt, M. Chmielus, Density variation in binder jetting 3D-printed and sintered Ti-6Al-4V, Addit. Manuf. 22 (2018) 746–752, https://doi.org/10.1016/j.addma.2018.06.017.
[5] E.A. Olevsky, R.M. German, Effect of gravity on dimensional change during sintering - I. shrinkage anisotropy, Acta Mater. 48 (2000) 1153–1166, https://doi.org/10.1016/S1359-6454(99)00368-7.
[6] E. Torresani, R.M. German, R. Huff, E.A. Olevsky, Influence of gravity on sintering of 3D-printed powder components, J. Am. Ceram. Soc. 105 (2022) 131–146, https://doi.org/10.1111/jace.18056.
[7] E.A. Olevsky, R.M. German, A. Upadhyaya, Effect of gravity on dimensional change during sintering - II. Shape distortion, Acta Mater. 48 (2000) 1167–1180, https://doi.org/10.1016/S1359-6454(99)00369-9.
[8] E.A. Olevsky, Theory of sintering: from discrete to continuum, Mater. Sci. Eng. R Rep. 23 (1998) 41–100, https://doi.org/10.1016/S0927-796X(98)00009-6.
[9] E. Torresani, A. Cabo Rios, T. Grippi, A.L. Maximenko, M. Zago, I. Cristofolini, E. A. Olevsky, Sintering model for predicting distortion of additively manufactured complex parts, Rapid Prototyp, J. 30 (2024) 369–383, https://doi.org/10.1108/RPJ-05-2024-0231.
[10] B.J. Paudel, D. Conover, J.K. Lee, A.C. To, A computational framework for modeling distortion during sintering of binder jet printed parts, J. Micromech. Mol. Phys. 6 (2021) 95–102, https://doi.org/10.1142/S2424913021420082X.
[11] S. Sadeghi Borujeni, A. Shad, K. Abburi Venkata, N. Günther, V. Ploshikhin, Numerical simulation of shrinkage and deformation during sintering in metal binder jetting with experimental validation, Mater. Des. 216 (2022) 110490, https://doi.org/10.1016/j.matdes.2022.110490.
[12] S. Sadeghi Borujeni, G.S. Saluja, V. Ploshikhin, Compensation of sintering deformation for components manufactured by metal binder jetting using numerical simulations, rapid prototype, Journal 29 (2023) 612–625, https://doi.org/10.1108/RPJ-06-2022-0181.
[13] K. Zhang, W. Zhang, R. Brune, E. Herderick, X. Zhang, J. Cornell, J. Forsmark, Numerical simulation and experimental measurement of pressureless sintering of stainless steel part printed by binder jetting additive manufacturing, Addit. Manuf. 47 (2021) 102330, https://doi.org/10.1016/j.addma.2021.102330.
[14] Z.J. Li, P. Xiao, H.L. Dai, Y. Yao, W.F. Luo, Modelling of geometrical deformation and compensation during sintering of binder jetting, Virtual Phys. Prototyp. 20 (2025) 1–21, https://doi.org/10.1080/17452759.2024.2443958.
[15] M. Sahli, A. Lebied, J.C. Gelin, T. Barrière, B. Necib, Numerical simulation and experimental analysis of solid-state sintering response of 316 L stainless steel micro-parts manufactured by metal injection molding, Int. J. Adv. Manuf. Technol. 79 (2015) 2079–2092, https://doi.org/10.1007/s00170-015-6983-8.
[16] J. Song, T. Barriere, B. Liu, J.C. Gelin, G. Michel, Experimental and numerical analysis on sintering behaviours of injection moulded components in 316L stainless steel powder, Powder Metall. 53 (2010) 295–304, https://doi.org/10.1179/003258908X334212.
[17] A. Cabo Rios, E. Hryha, E. Olevsky, P. Harlin, Sintering anisotropy of binder jetted 316L stainless steel: part I–sintering anisotropy, Powder Metall. (2021), https://doi.org/10.1080/00325899.2021.2020485.
[18] A. Cabo Rios, E. Hryha, E. Olevsky, P. Harlin, Sintering anisotropy of binder jetted 316L stainless steel: part II–microstructure evolution during sintering, Powder Metall. (2021), https://doi.org/10.1080/00325899.2021.2020486.
[19] A. Cabo Rios, E. Hryha, E. Olevsky, M. Persson, Modelling of delta-ferrite transformation effect on the sintering behavior of 316L binder jetting components. World PM2022 Proceeding, EPMA, 2022, https://doi.org/10.59499/WP225371818.
[20] A. Cabo Rios, E. Olevsky, E. Hryha, M. Persson, R.K. Bordia, Analytical models for initial and intermediate stages of sintering of additively manufactured stainless steel, Acta Mater. 249 (2023) 118822, https://doi.org/10.1016/j.actamat.2023.118822.
[21] T. Dahmen, N.G. Henriksen, K.V. Dahl, A. Lapina, D.B. Pedersen, J.H. Hattel, T. L. Christiansen, M.A.J. Somers, Densification, microstructure, and mechanical properties of heat-treated MAR-M247 fabricated by Binder Jetting, Addit. Manuf. 39 (2021), https://doi.org/10.1016/j.addma.2021.101912.
[22] M. Zago, G. Segata, M. Perina, A. Molinari, Binder jet 3D printing of 316L stainless steel: a Taguchi analysis of the dependence of density and mechanical properties on the printing parameters, J. Mater. Res. Technol. 34 (2025) 337–347, https://doi.org/10.1016/j.jmrt.2024.12.052.
[23] M. Zago, M. Perina, I. Cristofolini, Influence of geometry and printing parameters on the dimensional and geometrical accuracy of 316L binder jetting green product, Int. J. Interact. Des. Manuf. (2025), https://doi.org/10.1007/s12008-025-02390-8.
[24] T. Grippi, E. Torresani, A. Cabo Rios, A.L. Maximenko, M. Zago, I. Cristofolini, A. Molinari, R.K. Bordia, E.A. Olevsky, Mitigation of gravity-induced distortions of binder-jetting components during rotational sintering, Addit. Manuf. Lett. 10 (2024) 100215, https://doi.org/10.1016/j.addlet.2024.100215.
[25] J. Meng, N.H. Loh, B.Y. Tay, G. Fu, S.B. Tor, Tribological behavior of 316L stainless steel fabricated by micro powder injection molding, Wear 268 (2010) 1013–1019, https://doi.org/10.1016/j.wear.2009.12.033.
[26] M. Fellah, M. Labaïz, O. Assala, A. Iost, L. Dekhil, Tribological behaviour of AISI 316L stainless steel for biomedical applications, Tribol. Mater. Surf. Interfaces 7 (2013) 135–149, https://doi.org/10.1179/1751584X13Y.0000000032.
[27] I. Velkavrh, F. Ausserer, S. Klien, J. Voyer, A. Ristow, J. Brenner, P. Forêt, A. Diem, The influence of temperature on friction and wear of unlubricated steel/steel contacts in different gaseous atmospheres, Tribol. Int. 98 (2016) 155–171, https://doi.org/10.1016/j.triboint.2016.02.022.
[28] V. Vishnu, T.R. Prabhu, M. Imam, K.P. Vineesh, High-temperature dry sliding wear behavior of additively manufactured austenitic stainless steel (316L), Wear 540–541 (2024) 205259, https://doi.org/10.1016/j.wear.2024.205259.
[29] C.R. Alberto, E.A. Olevsky, E. Hryha, M. Persson, Modelling of δ-ferrite transformation effect on the sintering behaviour of 316L binder jetted components, WorldPM 2022 (2022).
[30] B. Barthel, F. Janas, S. Wieland, Powder condition and spreading parameter impact on green and sintered density in metal binder jetting, Powder Metall. 0 (2021) 1–9, https://doi.org/10.1080/00325899.2021.1912923.
[31] U. Hofmann, J. Ferchow, M. Meboldt, Evaluating effect of manufacturing process on design in metal binder jetting, results eng. 24 (2024) 103430. https://doi.org/10.1016/j.rineng.2024.103430.

[32] M. Zago, G. Segata, M. Perina, I. Cristofolini, Assessment of causes of precision and accuracy loss in metal binder jetting additive manufacturing technology, J. Manuf. Mater. Process. 9 (2025) 363, https://doi.org/10.3390/jmmp9110363.
[33] M. Dorula, M. Khademitab, M. Jamalkhani, A. Mostafaei, Location dependency of green density and dimension variation in binder jetted parts, Int. J. Adv. Manuf. Technol. 132 (2024) 2853–2861, https://doi.org/10.1007/s00170-024-13529-4.
[34] A. Mostafaei, P. Rodriguez De Vecchis, I. Nettleship, M. Chmielus, Effect of powder size distribution on densification and microstructural evolution of binder-jet 3D-printed alloy 625, Mater. Des. 162 (2019) 375–383, https://doi.org/10.1016/j.matdes.2018.11.051.
[35] A. Cabo Rios, T. Mishurova, L. Cordova, M. Persson, G. Bruno, E. Olevsky, E. Hryha, Ex-situ characterization and simulation of density fluctuations evolution during sintering of binder jetted 316L, Mater. Des. 238 (2024) 112690, https://doi.org/10.1016/j.matdes.2024.112690.
[36] E. Wheat, M. Vlasea, J. Hinebaugh, C. Metcalfe, Sinter structure analysis of titanium structures fabricated via binder jetting additive manufacturing, Mater. Des. 156 (2018) 167–183, https://doi.org/10.1016/j.matdes.2018.06.038.
[37] S. Bafaluy Ojea, J. Torrents-Barrena, M.T. Pérez-Prado, R.M. Moreno, F. Sket, Binder jet green parts microstructure: advanced quantitative analysis, J. Mater. Res. Technol. 23 (2023) 3974–3986, https://doi.org/10.1016/j.jmrt.2023.02.051.
[38] M. Zago, N. Lecis, M. Mariani, I. Cristofolini, Analysis of the causes determining dimensional and geometrical errors in 316L and 17-4PH stainless steel parts fabricated by metal binder jetting, Int. J. Adv. Manuf. Technol. 132 (2024) 835–851, https://doi.org/10.1007/s00170-024-13437-7.
[39] N.D. Parab, J.E. Barnes, C. Zhao, R.W. Cunningham, K. Fezzaa, A.D. Rollett, T. Sun, Real time observation of binder jetting printing process using high-speed X-ray imaging, Sci. Rep. 9 (2019) 1–10, https://doi.org/10.1038/s41598-019-38862-7.
[40] D. Yamaguchi, N. Oya, X-ray observation study of the influence of binder deposition on sintering process of aluminum binder jetting, Int. J. Adv. Manuf. Technol. 128 (2023) 1981–1990, https://doi.org/10.1007/s00170-023-12058-w.
[41] M. Ziaee, N.B. Crane, Binder jetting: a review of process, materials, and methods, Addit. Manuf. 28 (2019) 781–801, https://doi.org/10.1016/j.addma.2019.05.031.
[42] J. Kráľ, T. Dzuro, H. Debski, Applying binder jetting technology to 316L stainless steel materials and testing its mechanical and dimensional properties depending on the printing method, Materials (2024) 17, https://doi.org/10.3390/ma17174400.
[43] Simufact Additive, Accelerating the metal binder jetting workflow with sintering simulation, Met. Addit. Manuf. Inovar. Commun. Ltd. (2021) 165–172. https://www.metal-am.com/metal-additive-manufacturing-magazine/.
[44] PROTO3000, Metal binder jetting 3D printing design guidelines. https://proto3000.com/service/3d-printing-services/materials/overview/design-guidelines/metal-binder-jetting/, 2024 (accessed November 27, 2024).
[45] Desktop Metal, Laser-free metal 3D printing with binder Jetting technology. https://www.desktopmetal.com/resources/metal-3dprinting-binder-jetting-guide, 2023 (accessed November 27, 2024).
[46] M. Schmidt-Lehr, T. Führer, Design guideline for sinter-based additive manufacturing, AM Power Insights 8 (2021).